Electronic Supplementary Material (ESI) for Catalysis Science & Technology.

Electronic Supporting Information File

Nano-engineered hierarchical porous silicas for enhanced catalytic efficiency in liquid phase.

A. Zaki[a,d], M. Wastiaux[a], S.Casale[b], A. Mussi[c], J.F. Dhenin[c], C. Lancelot[a], J.P. Dacquin[a]*and P. Granger[a]*

[a] Univ. Lille, CNRS, Centrale Lille, ENSCL, Univ. Artois, UMR 8181 - UCCS - Unité de Catalyse et Chimie du Solide, F-59000 Lille, France

[b] Univ Pierre et Marie Curie, CNRS, UMR 7197-LRS- Laboratoire de Réactivité et Surface, Paris, France.

[c]Univ Lille, CNRS, UMR8207-UMET- Unité Matériaux et Transformations, F-59000 Lille, France

[d]CIC EnergiGUNE, 01510 Minano (Alava) Spain

Summary

1. Experimental

1.1. Preparation of 1 wt.%Pt/SiO$_2$

Tunable macroporous-mesoporous silica catalyst supports (called "D-m$_{\text{channel}}$" for Donut-like macrostructure with mesoporous channels and "H-m$_{\text{hole}}$" for Honeycomb-like macrostructure with hole-like mesopores) were prepared on a gram-scale according to an adapted dual-templating method (*see the reference : A. Zaki, J. Xu, G. Stoclet, S. Casale, J.P. Dacquin, P. Granger, Mic. Mes. Mat., 2015, 208, 140-151*). This templating method involves the direct insertion of the macrotemplate (polymer spheres) in the solution following the addition of TEOS and block-copolymer to structure the mesoporous network. The prehydrolysed precursor solution subsequently impregnate the polymer spheres during one day and the *in situ* sol-gel transformation is obtained following hydrothermal treatment with different aging time (24h (*donut-like morphology*) or 96h (*honeycomb morphology*) and temperature (80°C), resulting in an intermediate composite nanospheres/P123-silica structure. Hybrid materials were calcined at 550°C (0.5°C.min^{-1}) to remove the organic porogens and to generate the final siliceous solids. Pure mesoporous solids have been prepared following the same method without addition of polymer spheres. All siliceous materials were impregnated by hexachloroplatinic acid solutions with adjusted concentrations in order to obtain 1 wt.% Pt. The precursors thus obtained were calcined in air at 400°C and successively reduced at 300°C in pure H$_2$ overnight.

1.2. Physicochemical characterization

Low angle X-ray diffraction patterns were recorded on a D8 advance X-ray diffractometer (Bruker AXS) running in Bragg-Brentano geometry fitted with a LynxEye Super Speed detector. XRD data were collected with Cu Kα radiation ($\lambda = 0.154$ nm, 40 kV, 30 mA) in the

0.3–6.0° 2Θ range with a 0.02° 2Θ step. Textural properties of mesopores for all materials were carried out on an automated gas adsorption analyzer (Tristar 3020). Prior to nitrogen physisorption measurements the calcined samples were pre-activated in vacuum at 150°C for 3 hours. The multipoint surface area was evaluated with the Brunauer-Emmett-Teller (BET) method over the range $P/P_0 = 0.075–0.35$ and pore size distribution was determined using the Barrett-Joyner-Halenda (BJH) method from the desorption isotherm branch. Total pore volume was calculated from the volume adsorbed at $P/P_0 = 0.99$. Material's porosity was assessed by textural analysis of both macropores and mesopores using mercury porosimetry (Micromeritics, Autopore III). Porosity values were obtained from the maximum amount of Hg introduced in the macro- and/or mesopores.Transmission Electron Microscopy measurements were performed on a JEOL JEM 2011 (LaB6) operating at 200 kV while scanning emission microscopy (Hitachi SU-70, SEM-FEG) was used for macrostructure analysis of all samples. Tilted series for tomographic analysis were acquired on a FEI Tecnai G2 20 microscope equipped with a LaB_6 crystal and operating at a voltage of 200 kV. Data acquisition and treatment (reconstruction and visualization) were performed on Digital Micrograph and ImageJ softwares. Hydrogen chemisorption measurements were carried out in a Micromeritics Autochem II 2920 apparatus (5 vol.% H_2/Ar). Prior to H_2 chemisorption, samples (100 mg) were *in situ* reduced at 300°C or 450°C for 1 hour under a flow of pure hydrogen (30 mL/min), then outgassed in flowing Ar at 400°C during one hour and finally cooled at ambient temperature. A series of pulses (5%H_2/Ar corresponding to 20 μL) was performed on the sample at ambient temperature until saturation.

1.3. Catalytic reaction

Preparation of the catalyst grain size:

From both dynamic light scattering analysis and scanning electron microscopy, our silica supports are finely divided powders which have a median particle diameter from about 200nm to 50 micrometers. In order to reach a mean particle diameter of 300 micrometers, silica pellets are prepared by carefully compressing silica powder with a FTIR pellet press. Pellets are subsequently dried at 120°C. Then, after several steps of mortaring, 2 stainless-steel test sieves with pore diameters of 350 and 250 micrometers are used to finally isolate the particles used for the catalytic reaction.

Hydrogenation reaction

Hydrogenation was performed at 20°C under stirring using 0.08 g of catalyst, 50 mL of deionized water and NO_2^- concentration of 100mg/L. Aliquots of 1 mL were regularly sampled and analyzed by ionic chromatography using a Methrom (844 UV/VIS Compact IC) equipped with a Metrosep A Supp 16 – 150/4.0 column. The catalytic nitrite reduction was studied at 20±0.5 °C in a semi-batch reactor continuously stirred. Ultrapure water was used throughout the experiment for preparing the standard as well as eluents in order to avoid the influence of any residual ions on the activity and selectivity measurement of the current study. 80 mg of catalyst in powder form with an average grain size of 300 μm was charged into the reaction vessel suspended in a 50 mL of potassium nitrite solution submitted to a continuous feed of gaseous hydrogen. Pure hydrogen gas was passed over the catalyst for 1 hour at 200 mL/min under magnetic stirring of 1000 rpm. While keeping the reaction vessel under inert atmosphere, 40 ml of the degassed ultra-pure water was added, stirred at 1000 rpm and the whole solution was purged with pure hydrogen gas at 100 ml/min for another 2 hours to remove any residual dissolved oxygen in water. To this, 10 ml of potassium nitrite solution was added to maintain an initial nitrite concentration of 100 ppm in the reaction medium. At periodic intervals samples were removed from the medium and analysed using ion chromatography for the nitrite (NaOH and Na_2CO_3 eluent) and ammonium ions (HNO_3 as eluent).

2. Results

2.1. SEM and TEM Analysis

Figure S1. Representative SEM micrographs of (a) Donut-like silica-P123 building blocks formed in the interstitial voids of sacrificial polymer spheres (before removal by calcination); (b) Donut-like macrostructure (*called D- for sample labelling*) obtained after calcination at 550°C under static air and (c) Honeycomb-like macrostructure (*called H- for sample labelling*) obtained after calcination at 550°C under static air

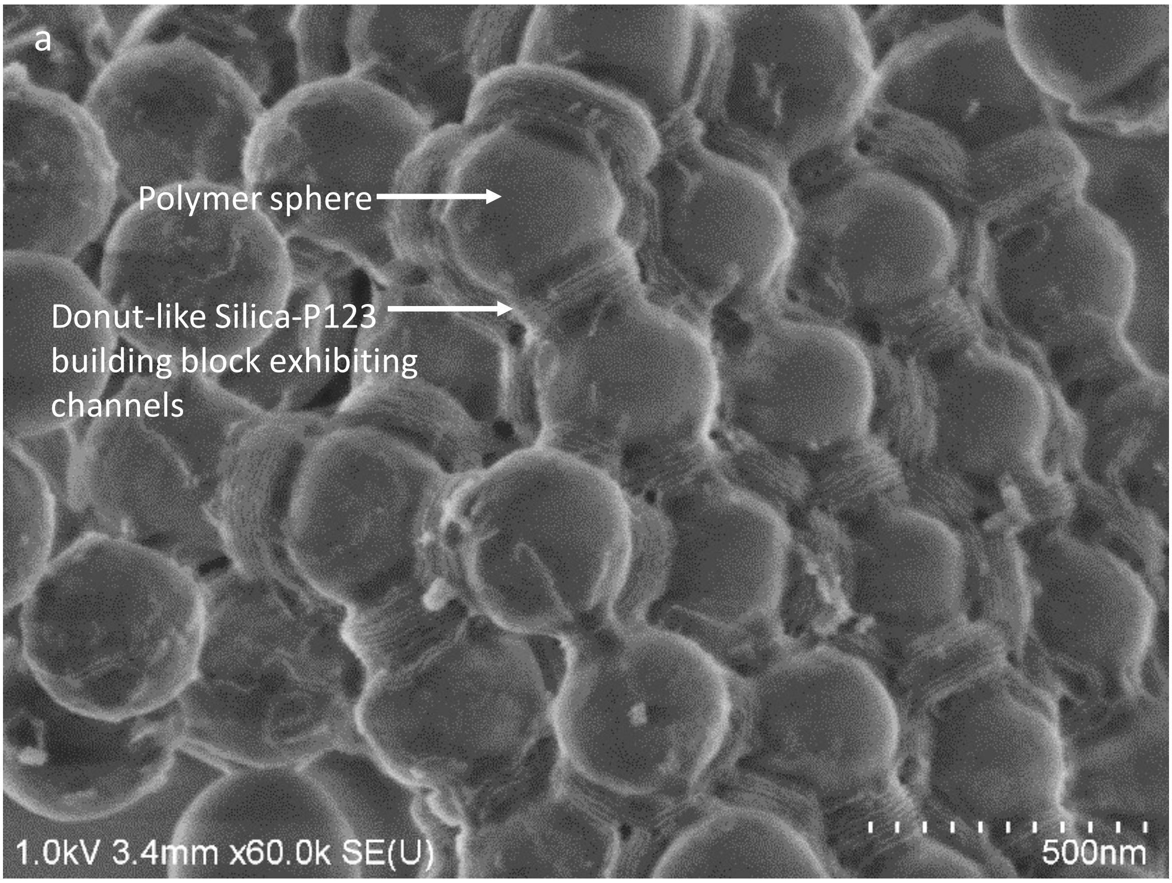

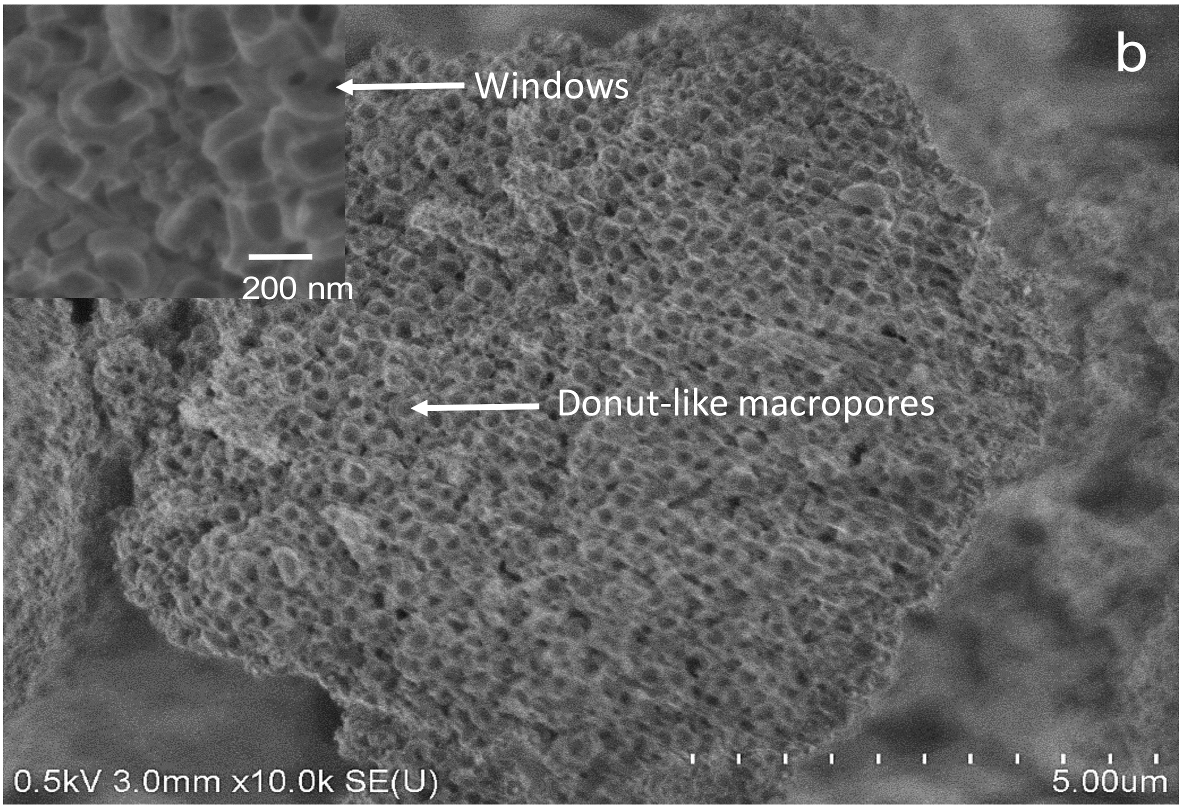
b
Windows
200 nm
Donut-like macropores
0.5kV 3.0mm x10.0k SE(U)
5.00um

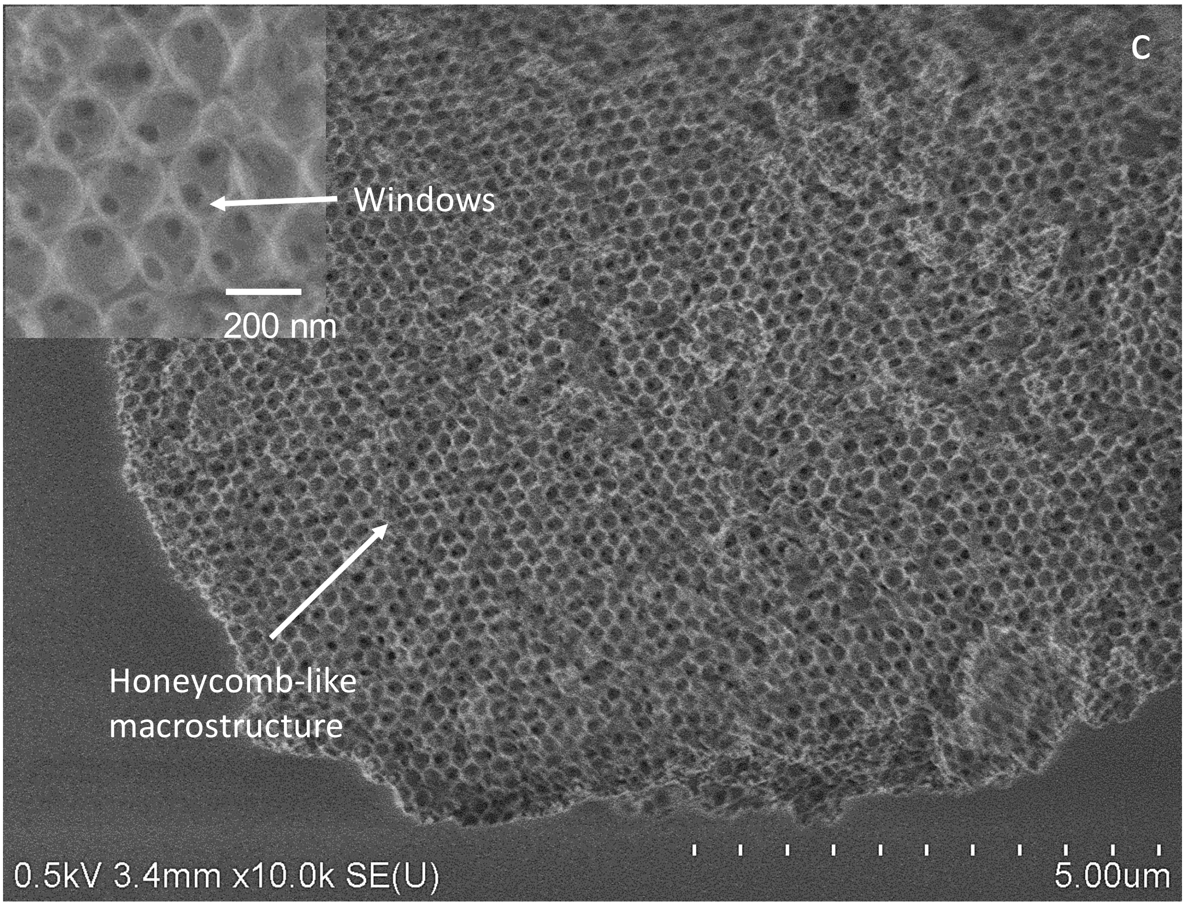
c
Windows
200 nm
Honeycomb-like macrostructure
0.5kV 3.4mm x10.0k SE(U)
5.00um

Figure S2. Representative TEM micrographs of (a) Donut-like macropores possessing (b) circular mesoporous channels running parallel to the main pore entrance (window or macroporous cavity); (c) Spherical macropores (honeycomb morphology) possessing (d) hole-like mesopores oriented randomly with the main pore entrance (window or macroporous cavity)

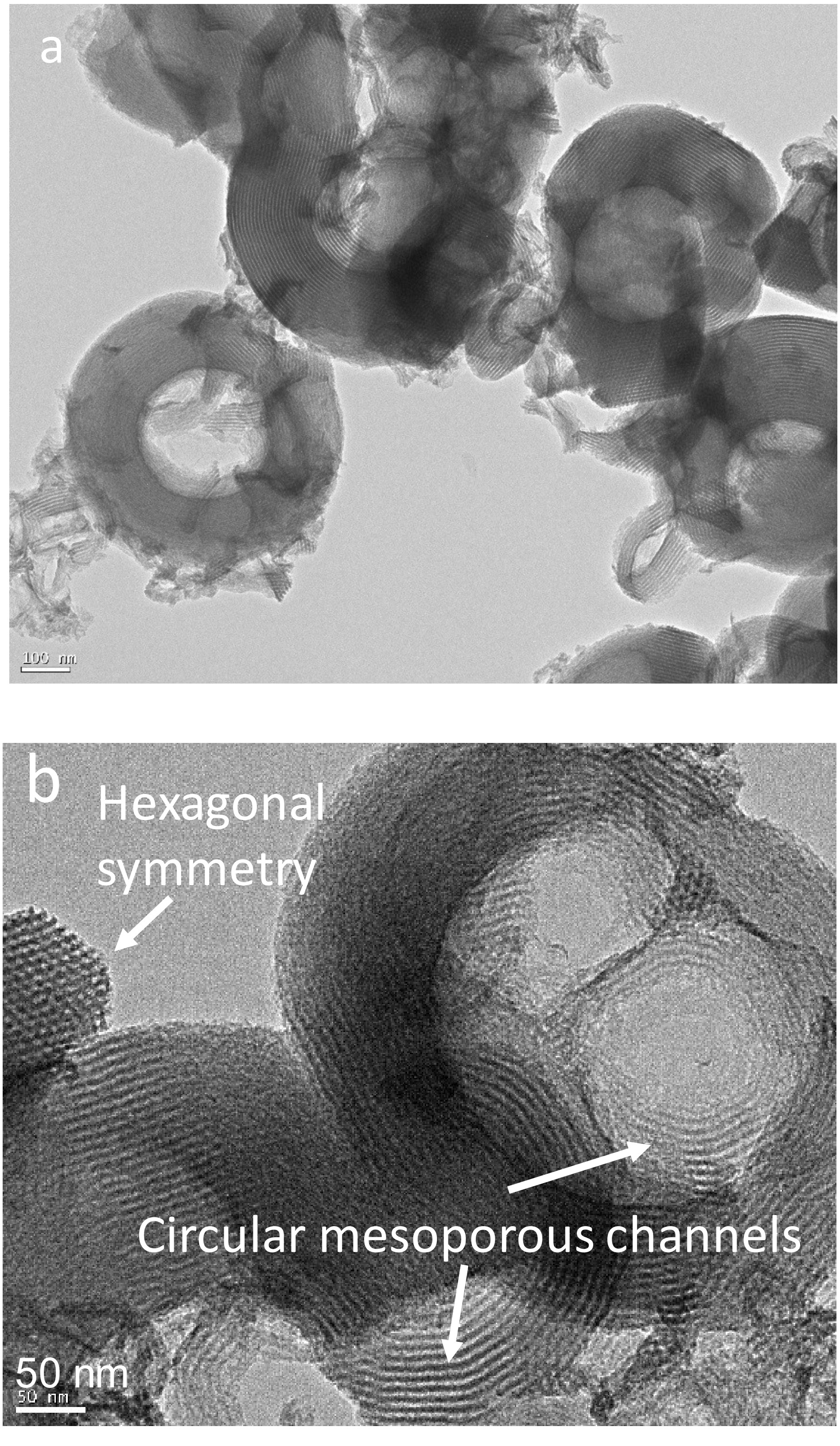

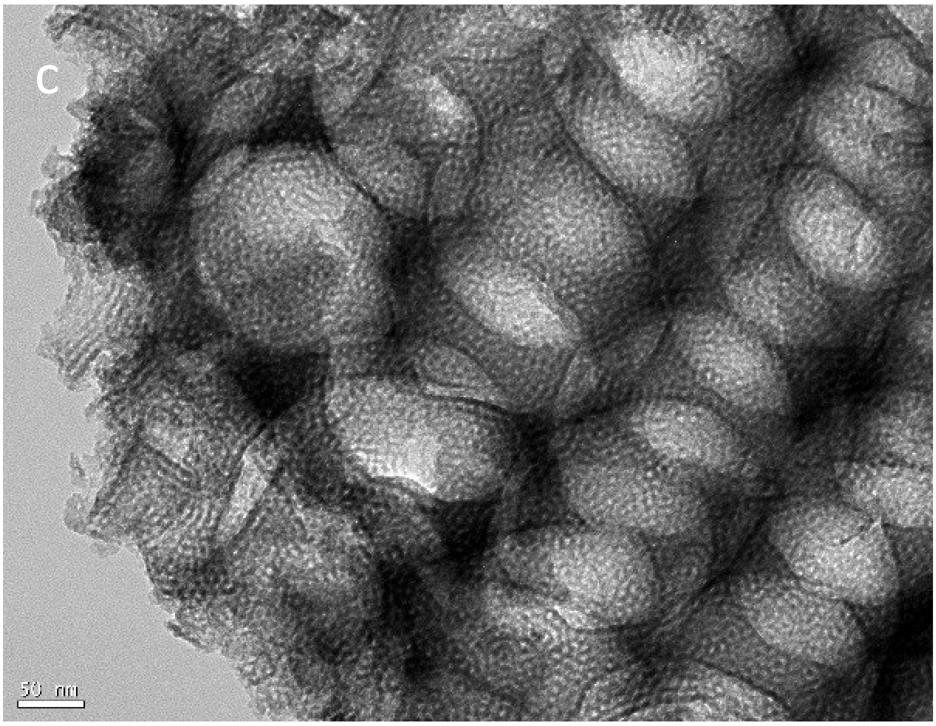
c
50 nm

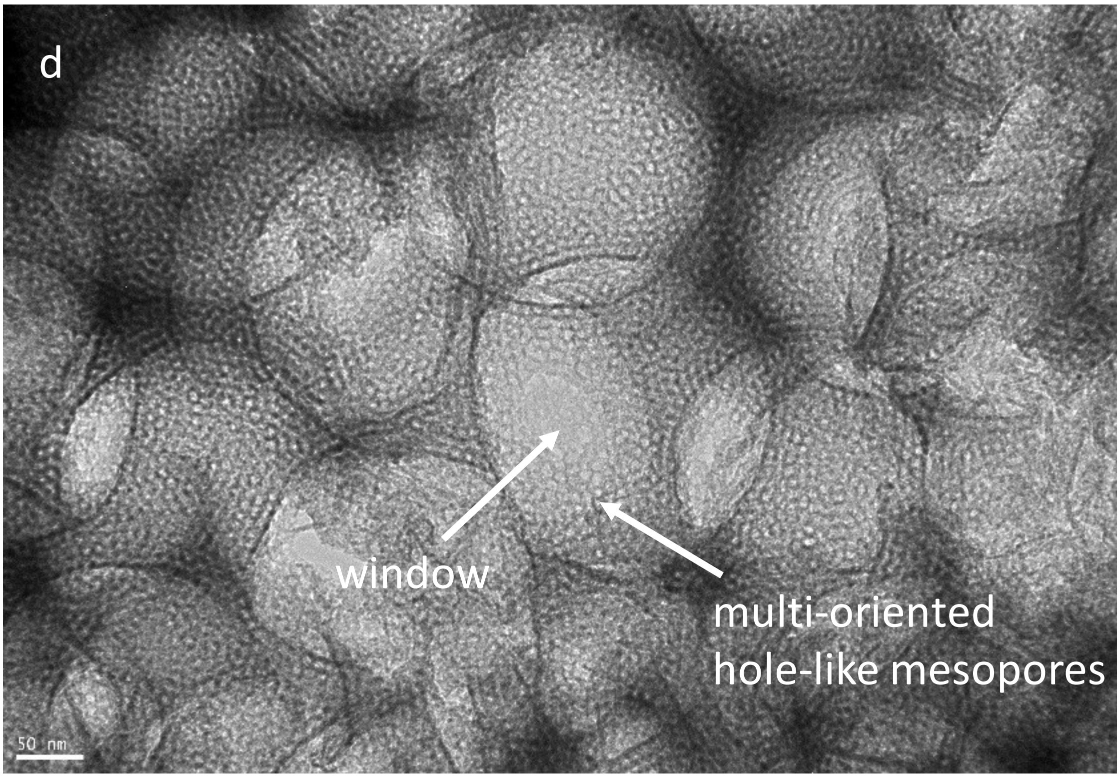
d
window
multi-oriented
hole-like mesopores
50 nm

2.2: Low angle XRD

Figure S3 : Low angle XRD patterns of (a) SBA-15, (b) Donut macrostructure (from 200nm polymer spheres imprinting) with mesoporous channels (***D-m*_channel-*200*** *as sample code*) and (c) Honeycomb macrostructure with hole-like mesopores (***H-m*_hole-*200*** *as sample code*)

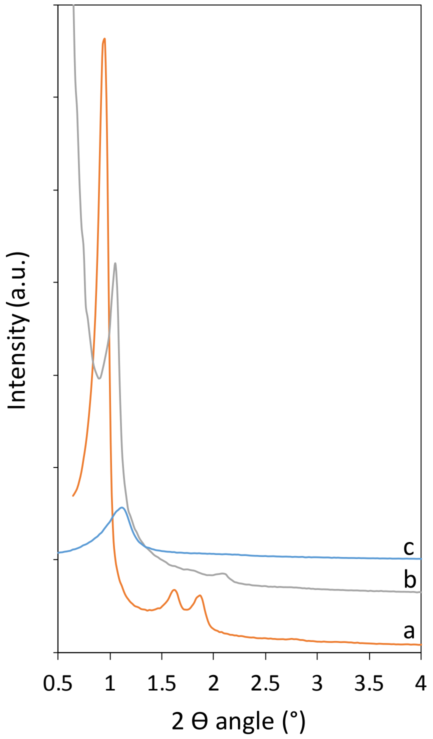

Morphological characteristics of the mesopores can be modified in our hierarchically porous systems, depending on the aging time applied during the synthesis of our hierarchical materials. When a short aging time is applied (24h), the Donut-like macrostructure is obtained and the mesopores formed are preferentially stabilized in the P6mm hexagonal mesostructure similar to the parent SBA-15 (see Fig S3a and S3b). The morphology of the Donut macropore induced a parallel alignment of mesoporous channels along the macropore surface with a circular shape. In contrary, when a longer aging time proceeds (96h), a honeycomb macrostructure is formed and mesopores are preferentially stabilized in a disordered hole structure. The configuration of the latter macroporous structure induced more constraints on the mesophase, leading to the partial loss of the hexagonally ordered arrays of the mesostructure (Figure S3c). It is noteworthy that the broadening of the main diffraction peak (100) obtained for Pt-H-m_{hole}-200 can be assigned to the stabilization of a smaller mesopore domain size with respect to Pt-SBA-15 and Pt-$Dm_{channel}$-200 catalysts. Thus, the macroporous honeycomb structure helped to break-up mesopore domain size with respect to the macroporous donut-like skeleton.

2.3. SEM-TEM Analysis on the (A) Pt-D-$m_{channel}$ and (B) Pt-H-m_{hole} series.

Figure S4: Representative SEM micrographs of the hierarchical macroporous mesoporous Pt-based catalysts (*sample codes: Pt-D-$m_{channel}$-X and Pt-H-m_{hole}-X with X corresponding to the sacrificial polymer sphere template used during the preparation*)

A. *(a) SBA-15, (b) Pt-D-$m_{channel}$-200, (c) Pt-D-$m_{channel}$-100, (d) Pt-D-$m_{channel}$-65*

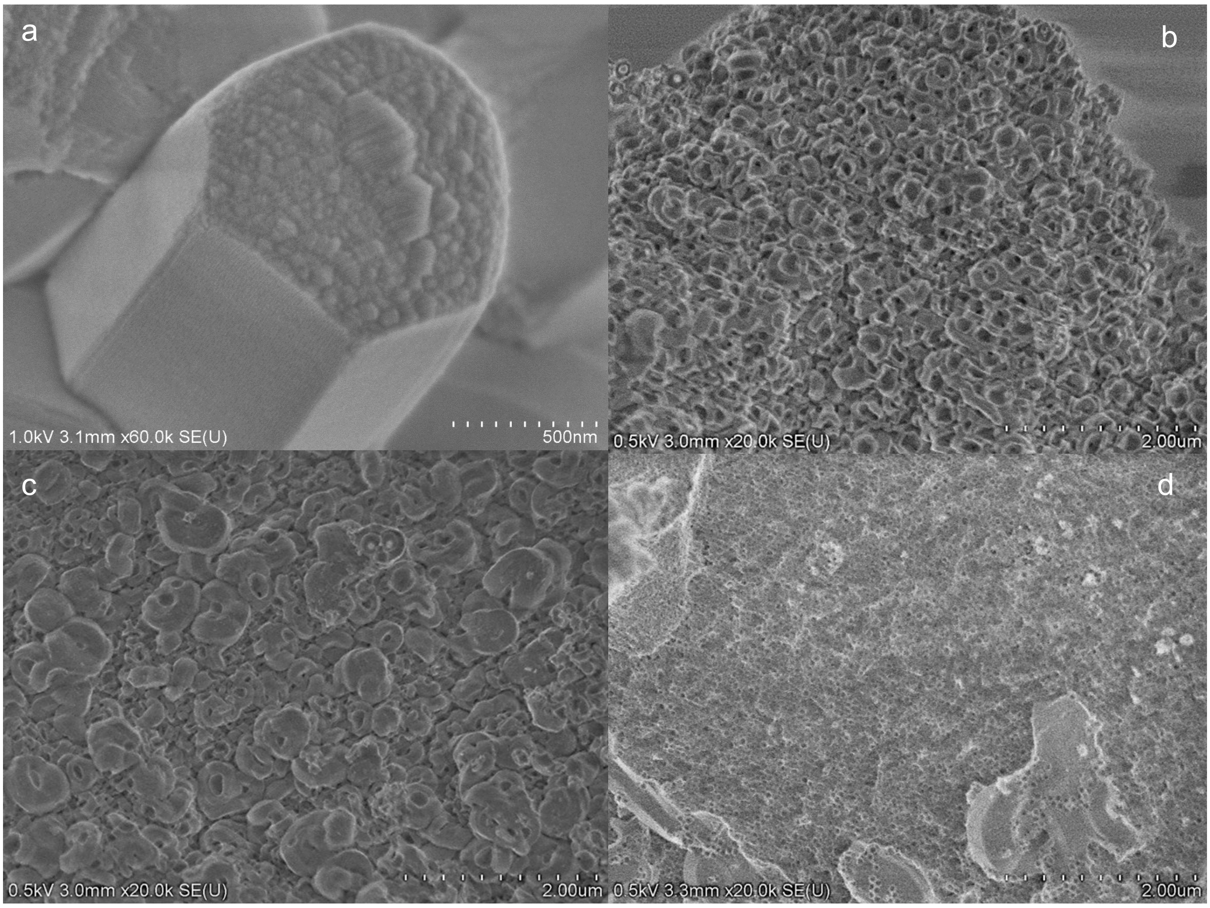

By shortening the aging time to 24h (at 80°C), random-like packing of macropores with donut-like morphology are obtained (b,c,d), namely Pt-Dm_{channel}-X series. Macroporosity is easily observed on all samples with respect to SBA-15. Isolated donut-like macropores are responsible of the preferential circular alignment of mesoporous channels along the macropore surface, inducing a clear change of the morphological characteristics of the mesopores with respect to Pt-H-m_{hole}-X series (see as well figure 1 and S1-S3). Residual content of SBA-15 rod-like grains are observed, particularly on Pt-D-$m_{channel}$-100 and Pt-D-$m_{channel}$-65.

B. *(a) SBA-15, (b) Pt-H-m_{hole}-200, (c) Pt-H-m_{hole}-100, (d) Pt-H-m_{hole}-65*

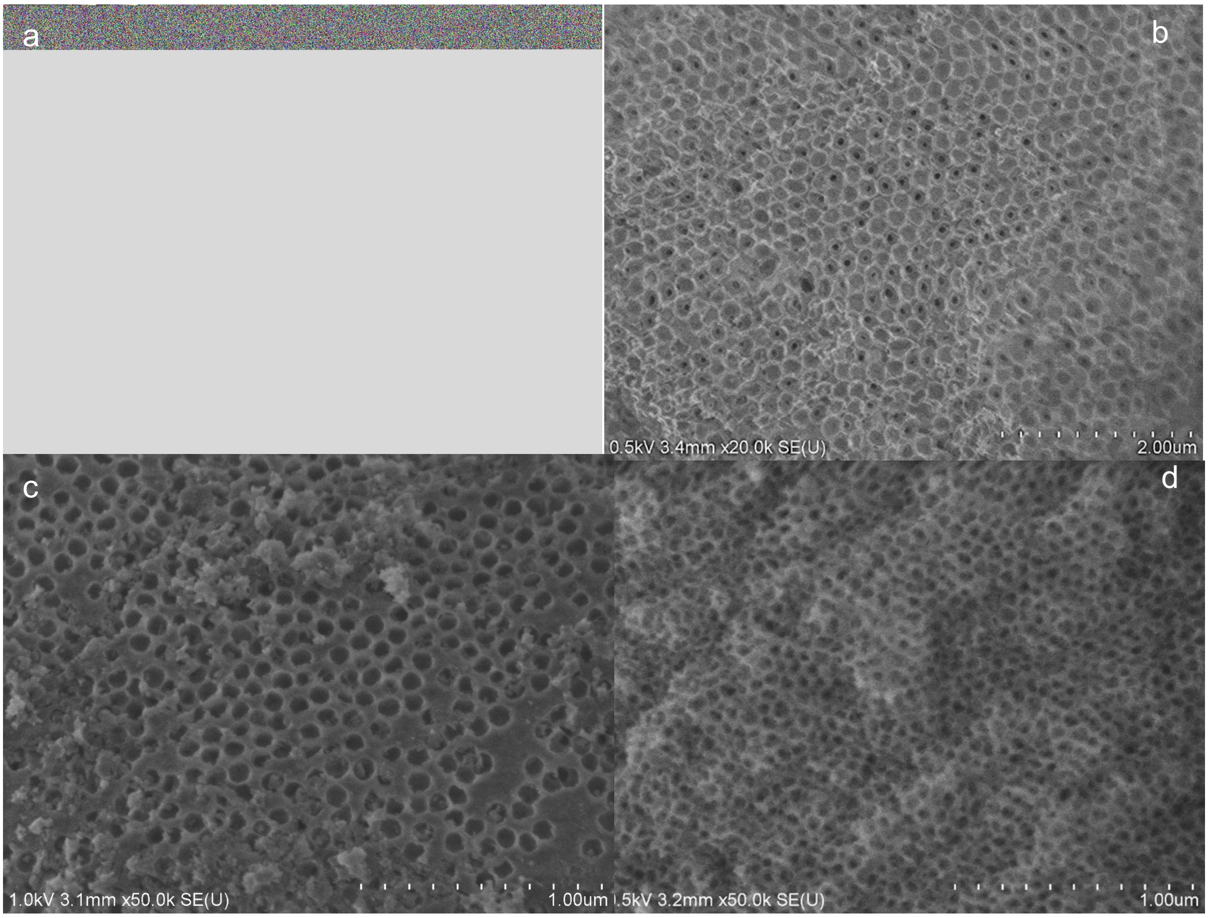

The Pt-H-m_{hole} series were obtained by dual-templating method involving the presence of polymer spheres with calibrated sizes (200, 100, 65 nm) and P123. After appropriate aging time (96h)/temperature (80°C) of the solution, complete change of the material's morphology occurred with respect to the rod-like morphology of SBA-15 (a). Clear honeycomb-like macrostructure is obtained whatever the size of the polymer spheres used during the synthesis (b,c,d). The best macrostructuration order is obtained for the Pt-H-m_{hole}-200 catalyst. The use of smaller polymer spheres imply the reduction of the macroporous wall thickness between adjacent macropores, inevitably leading to partial sintering of the macroskeleton in few areas.

2.4.Physical properties of the hierarchical bare supports (**D-m$_{channel}$-X and H-m$_{hole}$-X)**

Table S1. Physical properties of the bimodal-porous structure of silica supports (D-m$_{channel}$-X and H-m$_{hole}$-X where X is assigned to the polymer sphere size)

Catalyst	SSA ($m^2.g^{-1}$)	Total pore vol. ($cm^3.g^{-1}$)	Mesopore vol. ($cm^3.g^{-1}$)	Mesopore Size (nm)	Macropore Size (nm)
SBA-15	800	0.83	0.74	5.2	-
D-m$_{channel}$-65	743	1.78	1.71	4.3	46
D-m$_{channel}$-100	705	1.50	1.43	4.3	84
D-m$_{channel}$-200	607	0.74	0.67	4.3	142
H-m$_{hole}$-65	796	2.72	2.66	4.0	54
H-m$_{hole}$-100	983	2.10	2.04	3.9	78
H-m$_{hole}$-200	566	0.73	0.69	4.0	178

2.5. *Pt particle size distribution*

Figure S5: Representative TEM micrographs (microtome cutting) of the hierarchical macroporous mesoporous Pt-based catalysts. (a) Pt-D-$m_{channel}$-200 and (b) Pt-H-m_{hole}-200

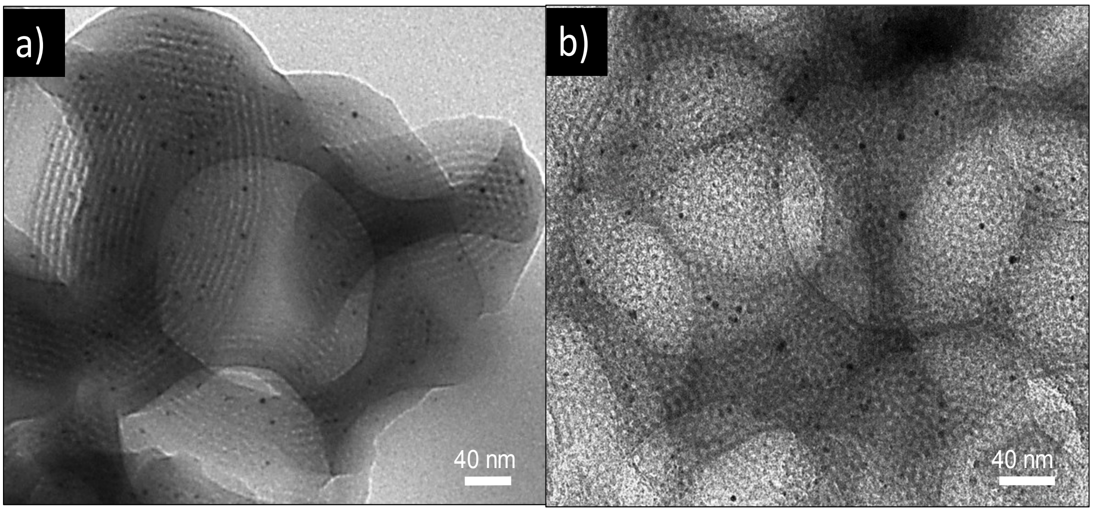

Figure S6: Particle size distribution profiles obtained from TEM Analysis and Image J measurements on 100 particles.

a) 1%Pt-SBA15

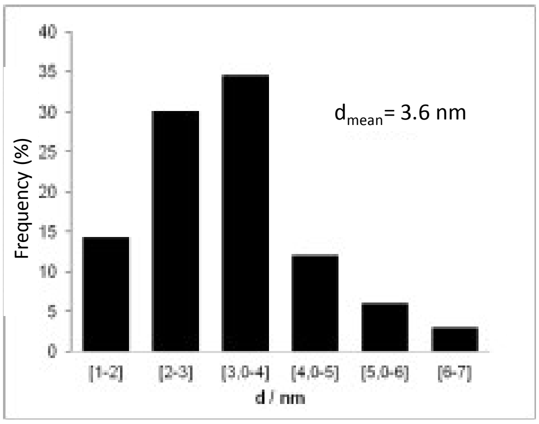

b) 1%Pt-$Dm_{channel}$-65

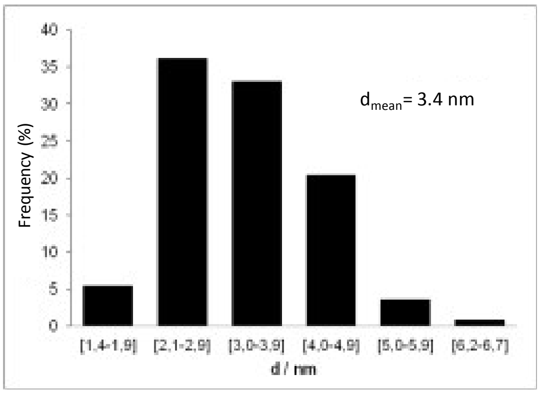

c) 1%Pt-$Dm_{channel}$-100

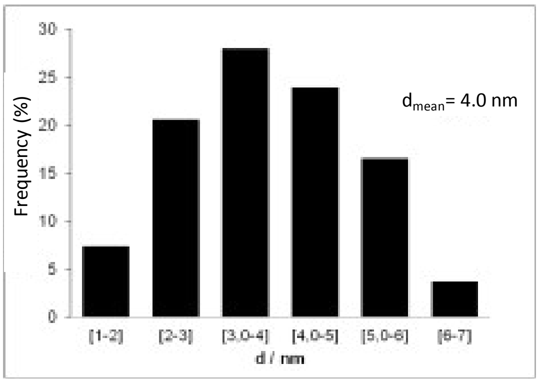

d) 1%Pt-Hm$_{hole}$-65

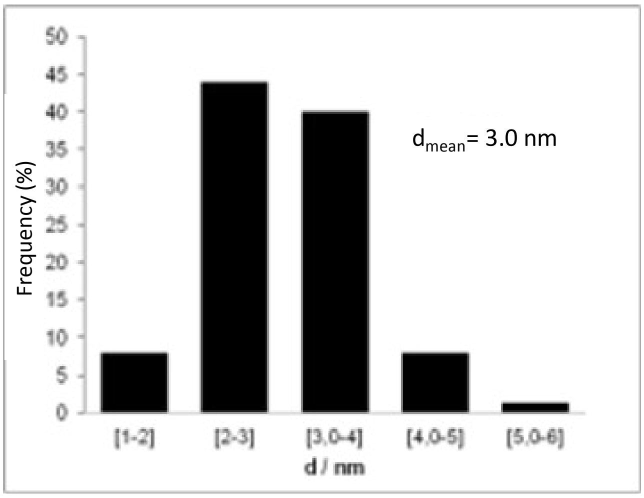

d) 1%Pt-Hm$_{hole}$-100

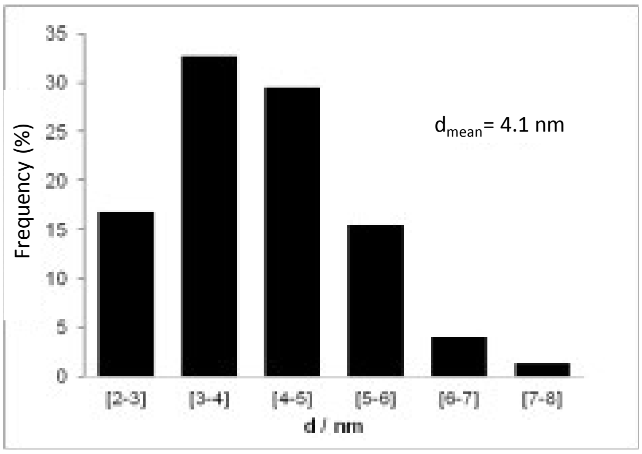

2.6. Tomography Analysis

One of the reconstructed tomograms obtained from tilted TEM images acquired on Pt-Hm_{hole}-200 solid is presented by a snapshot Fig. S7. Exact location of the Pt particles is further evidenced in the extracted slices from the tomogram, clearly showing the location of the platinum particles inside the mesoporous network of the support (Fig. S8 and see the attached video).

Figure S7. Reconstructed 3D tomogram of Pt-Hm_{hole}-200 (reduced at 300°C) obtained from the 2D projections obtained by TEM micrograph tilt series between -70° and + 70°.

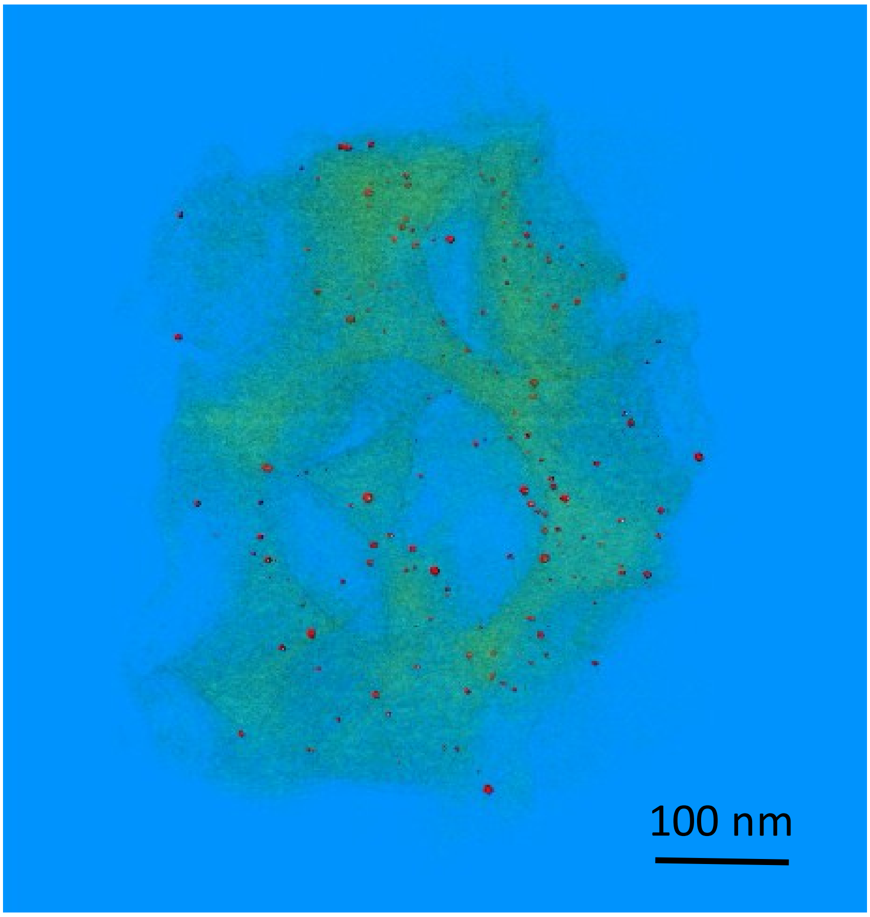

Fig. S8: Extracted slice of Pt-H-m_{hole}-200 catalyst (reduced at 300°C) from the reconstructed 3D tomogram

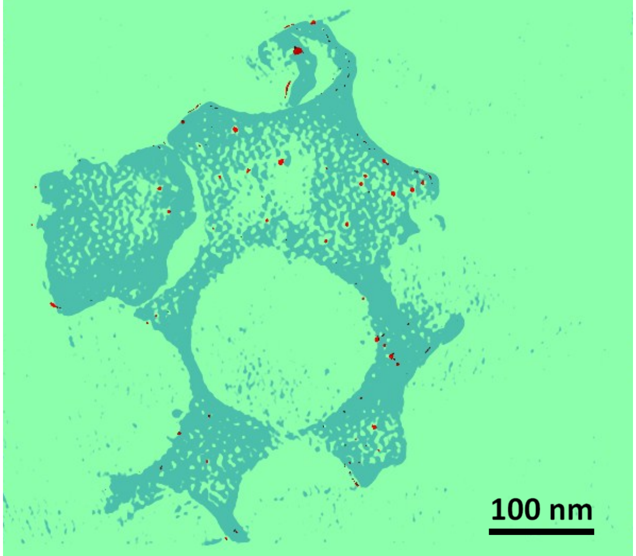

The identification of Pt particles inside the mesoporosity of the silica materials is strictly not possible using classical two-dimensional transmission electron microscopy. Assessment of the 3D localization of the Pt particles within the silica framework has been achieved through the use of 3D tomography electron microscopy that is able, after a quite long process, to isolate 3D mathematical objects representative of the sample. The advantage is that we can extract different slices from the 3D object and determine the precise localization of the metallic Pt particles. As illustrated in the 3D movie assigned to the Pt-H-m_{hole}-200 catalyst (available from the attached video), we clearly observe Pt particles preferentially coming out from mesoporous holes of the silica. However, particles located on the macropore surface cannot be ruled out, but correspond to a limited number of particles (around 5% in the studied objects) with respect to the particles inside the mesoporosity.

2.7. Textural characterization

Figure S9: (A) N_2 physisorption isotherms measured at -196°C and (B) pore size distribution on bare multiporous silica bare supports (red); and Pt-based catalysts (blue). (a) SBA-15 and Pt-SBA15; (b) D-$m_{channel}$-65 and Pt- D-$m_{channel}$-65; (c) D-$m_{channel}$-100 and Pt- D-$m_{channel}$-100; (d) D-$m_{channel}$-200 and Pt- D-$m_{channel}$-200; (e) H-m_{hole}-65 and Pt- H-m_{hole}-65; (f) H-m_{hole}-100 and Pt- H-m_{hole}-100; (g) H-m_{hole}-200 and Pt- H-m_{hole}-200.

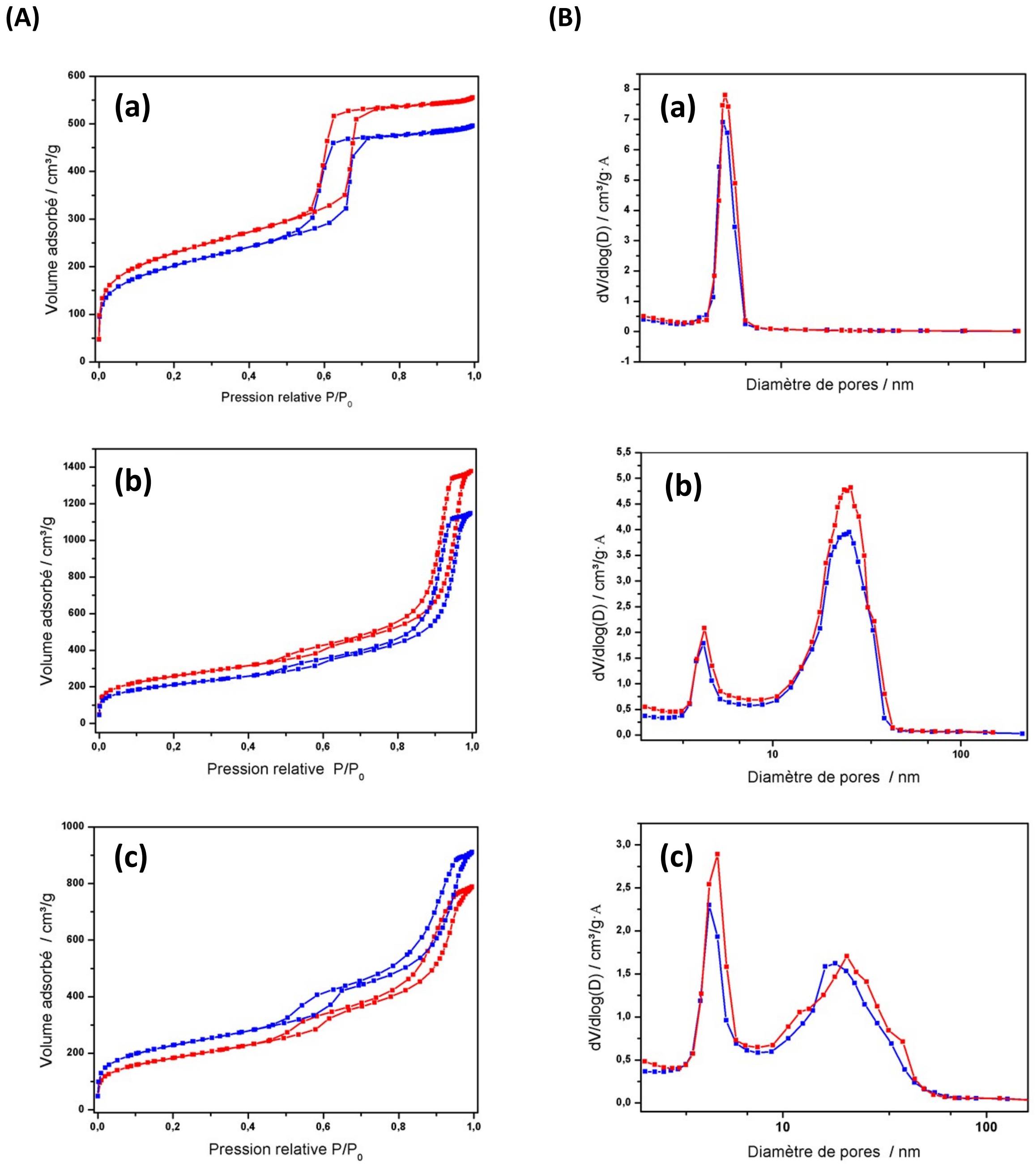

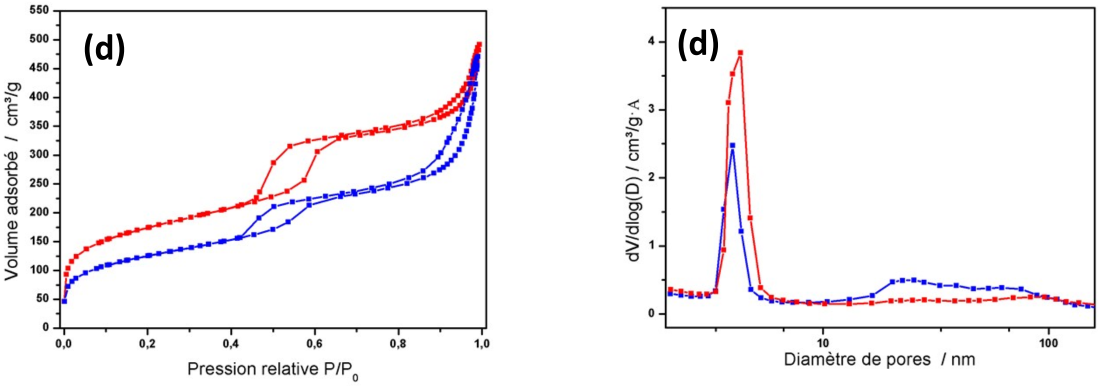

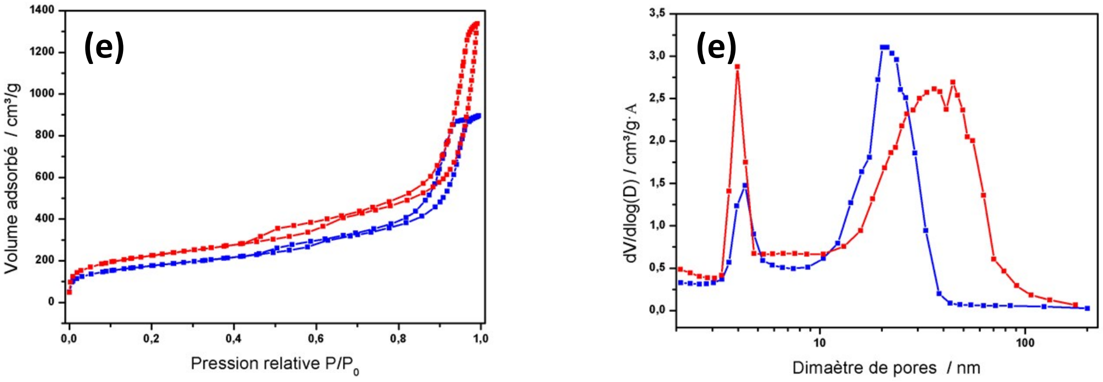

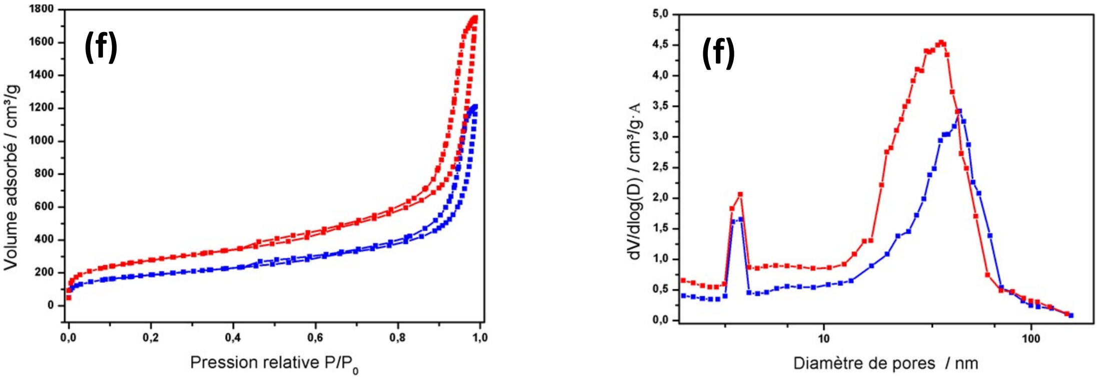

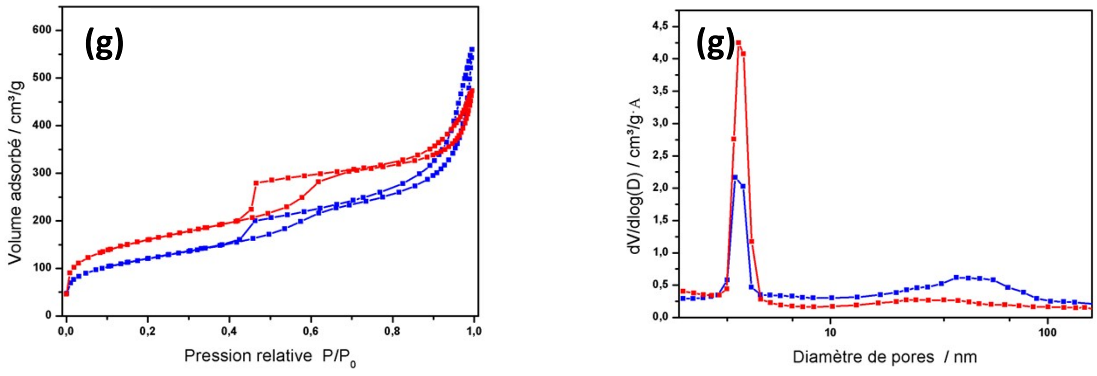

Nitrogen physisorption measurements were performed on bare silica calcined at 550°C in air before and after platinum incorporation. The specific surface area, pore volume and average pore size calculated by the BET and BJH methods are reported in Table S1 and Table 1. As illustrated above, the incorporation polymer spheres of well-defined size during the sol-gel synthesis process induce significant changes on the textural features. A classical H1 hysteresis loop is observed on the mesoporous SBA-15 materials whereas physisorption isotherms on silica samples obtained by using hard templates reveal a combination of type II and type IV isotherms, which characterizes the coexistence of macropore and mesopores networks. Such an observation matches properly with the slight decrease observed on the specific surface area (see Table S1). It is worthwhile to note that further impregnation and thermal treatment process after platinum incorporation via incipient impregnation did not lead to significant alteration ascribed to a collapse of the porous network or pore plugging indicating a high degree of platinum dispersion (Table 1)

2.8. Catalytic measurements

Fig. S10. Influence of external diffusion phenomena on the determination of initial rate for the reduction on nitrites to nitrogen with H_2 on Pt supported on none porous Silica aerosil catalyst in a semi-batch reactor according to the following experimental condition: T(reaction) = 20°C with 80 mg mass of powder catalyst with average grain size of 300 μm in contact with 50 mL of solution of nitrites (100 mg.L^{-1}) exposed to a continuous flow of hydrogen of 200 mL.min^{-1}.

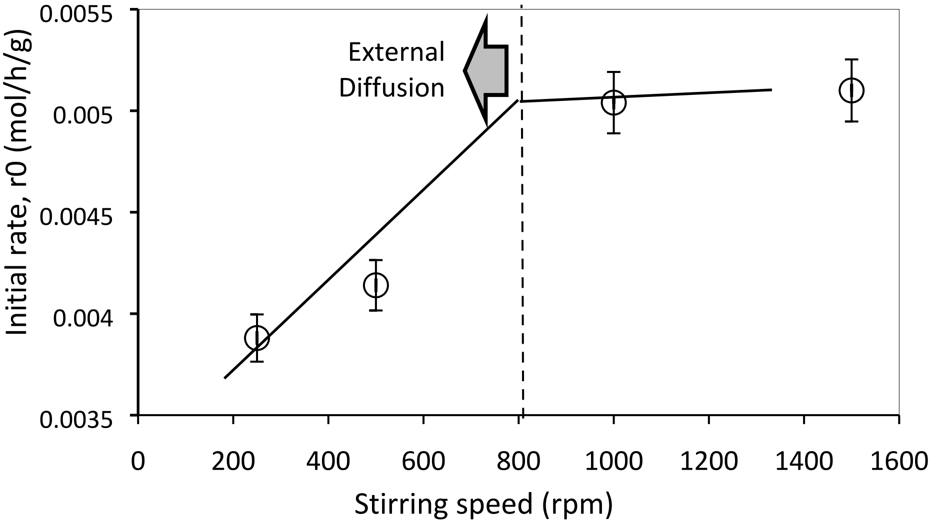

As observed, the reaction rate strongly increases from 200 rpm to 1000 rpm. Nevertheless, above 1000 rpm, the reaction rate is maintained at around 0.005 mol/h/g. Thus, a stirring speed of 1000 rpm was selected to remove the effects of external diffusion limitations.

2.9 Calculation of the effective diffusivities and Weisz-Prater criterion

To check the presence or not of internal diffusion limitations, we estimated the Weisz Prater criterion using the following equation:

$$C_{WP} = (r_{0.}\ \rho_{App}.\ Rp^2)/\ (C_{Sub}\ .\ D_{eff})$$

With:
r_0 : initial reaction rate in $mol.s^{-1}.g^{-1}$
Rp^2: Radius of the particle (cm^2)
C_{Sub}: Concentration of the substrate on the surface (in the absence of external diffusion, this value correspond to the bulk concentration of the species) ($mol.cm^{-3}$).
Herein $C_{NO2-} = 2.17\ 10^{-6}\ mol.cm^3$ and $C_{H2} = 6.24\ 10^{-7}\ mol.cm^{-3}$

D_{eff}: Effective diffusivity taking into account the porosity (ε) and the tortuosity (τ) of the material following the equation:

$$D_{eff} = D_{bulk}\ .\ \varepsilon\ /\ \tau$$

D_{bulk} is the bulk diffusivity ($cm^2.s^{-1}$)
$D_{bulk}NO_2^- = 1.91\ 10^{-5}\ cm^2.s^{-1}$
$D_{bulk}H_2 = 5.11\ 10\text{-}5\ cm^2.s^{-1}$.

ρ_{App} (apparent density): $\rho_{AppSBA} = 2.34$ (from Weinberger et al. Micro.Meso.Mater 2016)

ε is the porosity of the material. Porosity values were obtained from textural analysis of both macropores and mesopores by mercury porosimetry (Micromeritics, Autopore III) obtained from the maximum amount of Hg introduced in the macro- and/or mesopores.

τ is the tortuosity factor calculated from the relation : τ = 1 - ln ε (from Kolitcheff et al., Microporous and Mesoporous Materials 248 (2017) 91-98, Koza et al., Physical Review E 78026306 (2008)).

Table S2: Estimation of the effective diffusivities and Weisz Prater criterion

Sample	ε	τ	**D_{eff} NO_2^- ($cm^2.s^{-1}$)**	$WP_{NO_2^-}$	**D_{eff} H_2 ($cm^2.s^{-1}$)**	WP_{H2}
Pt-SBA	0.54	1.6	**$7.64\ 10^{-6}$**	3.3	**$1.72\ 10^{-5}$**	4.0
Pt-$Dm_{channel}$-200	0.77	1.3	**$1.16\ 10^{-5}$**	1.7	**$3.02\ 10^{-5}$**	2.3
Pt-$Dm_{channel}$-100	0.74	1.3	**$1.08\ 10^{-5}$**	1.1	**$2.91\ 10^{-5}$**	1.6
Pt-$Dm_{channel}$-65	0.72	1.3	**$1.06\ 10^{-5}$**	1.3	**$2.83\ 10^{-5}$**	1.7
Pt-Hm_{hole}-200	0.75	1.3	**$1.11\ 10^{-5}$**	4.7	**$2.94\ 10^{-5}$**	6.2
Pt-Hm_{hole}-100	0.77	1.3	**$1.46\ 10^{-5}$**	1.6	**$3.03\ 10^{-5}$**	4.4
Pt-Hm_{hole}-65	0.73	1.3	**$1.34\ 10^{-5}$**	4.2	**$2.87\ 10^{-5}$**	6.9

The calculated results indicate that WP values are very close to each other and above 1 for $NO_2^-$and H_2 , which suggest the presence of internal resistance in SBA-15 and derivated hierarchical materials. Regarding this simple estimation, the presence of macro- mesopores, which are responsible of the further opening of the materials porosity, do not permit to totally alleviate internal diffusion limitations within the grains of the hierarchical catalyst series. However, bearing in mind that most of the Pt particles are dispersed within the mesoporosity, this calculation does not take into account the mesopore domain sizes (i.e. length of the mesoporous channels) of the different porous materials. Typically, in our synthesis conditions, long mesoporous channels of SBA-15 can easily reach more than 1 μm in length (low angle XRD and figure S4) which can result in the decrease of accessible Pt particles located inside the pore channel. By breaking up the mesopore domain size, honeycomb macropores incorporation increase the density of accessible active sites by acting as large entrances. Moreover, regarding the figure 1 and figures S1 to S2, hole-like morphology of the mesopore entrance is critical and Pt-H-m_{hole}-X catalysts offer the possibility to give short diffusion paths, arising in a higher local density of active sites per mesopore volume with respect to Pt-D-$m_{channel}$ catalysts.